Zhao *et al. Microstructures* 2024;4:2024032
DOI: 10.20517/microstructures.2023.80

Microstructures

Research Article

Open Access

Check for updates

Computational exploration of two-dimensional vacancy-free boridene sheet and its derivatives: high stabilities and the promise for hydrogen evolution reaction

Yuying Zhao[1,#], Jincan Zhang[1,#], Fengxian Ma[1], Hongbo Wu[1], Weizhen Meng[1], Ying Liu[1], Yalong Jiao[1], Aijun Du[2]

[1]College of Physics, Hebei Key Laboratory of Photophysics Research and Application, Hebei Normal University, Shijiazhuang 050024, Hebei, China.
[2]School of Chemistry and Physics and Centre for Materials Science, Gardens Point Campus, Queensland University of Technology, Brisbane, QLD 4000, Australia.
[#]Authors contributed equally.

Correspondence to: Prof. Fengxian Ma, College of Physics, Hebei Key Laboratory of Photophysics Research and Application, Hebei Normal University, Shijiazhuang 050024, Hebei, China. E-mail: fengxianma@hebtu.edu.cn; Prof. Yalong Jiao, College of Physics, Hebei Key Laboratory of Photophysics Research and Application, Hebei Normal University, Shijiazhuang 050024, Hebei, China. E-mail: yalong.jiao@hebtu.edu.cn

How to cite this article: Zhao Y, Zhang J, Ma F, Wu H, Meng W, Liu Y, Jiao Y, Du A. Computational exploration of two-dimensional vacancy-free boridene sheet and its derivatives: high stabilities and the promise for hydrogen evolution reaction. *Microstructures* 2024;4:2024032. https://dx.doi.org/10.20517/microstructures.2023.80

Received: 1 Dec 2023 **First Decision:** 18 Jan 2024 **Revised:** 4 Feb 2024 **Accepted:** 19 Feb 2024 **Published:** 28 May 2024

Academic Editors: Yi Du, Junhao Lin **Copy Editor:** Fangyuan Liu **Production Editor:** Fangyuan Liu

Abstract

The recent synthesis of a two-dimensional (2D) MBene sheet, referred to as the boridene sheet ($Mo_4B_6T_z$), has ignited considerable interest in exploring 2D transition metal borides. Boridene has an ordered arrangement of metal vacancies, which are pivotal to its stability. Employing first-principles calculations, we explored the stable phases, electronic properties and catalytic abilities of boridene with different vacancy concentrations (V_m). Our results demonstrate that V_m significantly influences the cohesive energies of boridene sheets. Phonon spectrum and ab initio molecular dynamics simulations reveal the high stability of the vacancy-free boridene $Mo_6B_6T_6$ (T = O, -OH), underscoring their potential for experimental realization. Substituting Mo atoms with Nb, Ta, or W enhances the structural stability of boridene sheets, leading to the identification of four stable variants: $Nb_6B_6F_6$, $Ta_6B_6F_6$, $Ta_6B_6O_6$, and $W_6B_6O_6$. These boridene sheets exhibit metallic behavior, with five structures displaying near-zero Gibbs free energy for hydrogen atom adsorption, indicating their potential as catalysts for the hydrogen evolution

reaction. The uncovering of vacancy-free boridenes and their 2D derivatives greatly broadens the scope of the MBene family.

Keywords: 2D materials, boridene, first-principles calculations, hydrogen evolution reaction

INTRODUCTION

The emergence of graphene has spurred the exploration and production of numerous other two-dimensional (2D) materials[1-4]. These include transition metal carbides, nitrides, and carbides/nitrides, commonly known as MXenes, which present intriguing prospects for expanding the realm of 2D materials[5-8]. MXenes are a class of materials formed by selectively removing atomic layers from their parent "MAX" phase, where "M" represents a transition metal, "A" indicates an element predominantly from columns IIIA and IVA, and "X" denotes either carbon or nitrogen[9,10], with over 100 MXenes having been either theoretically predicted or experimentally synthesized. This growing repertoire of MXenes demonstrates their immense potential for diverse applications, such as transistors, batteries, and magnetism-based technologies[11-20]. In particular, they have found extensive use in catalytic applications such as hydrogen/oxygen evolution reactions, oxygen reduction reactions, nitrogen reduction reactions, CO_2 reduction reactions, and more[21-23].

The boom of MXenes has further inspired efforts to extend their composition beyond the carbon/nitrogen elements. This has resulted in the emergence of transition metal borides, also known as MBenes, in recent years[24-26]. MBenes are derived from ternary or quaternary MAB phases, with "B" representing the boron element, and they exhibit a diverse range of complex structures and stoichiometries[27]. Currently, several types of MBenes, such as Cr_2B_2 and Mo_2B_2, have been synthesized[28,29], and over 50 MBene candidates have been predicted[22]. They have displayed fascinating properties, including exceptional electrical conductivity, high mechanical strength and stability, and remarkable thermal conductivity[30-33]. Consequently, MBenes hold great promise in various fields such as batteries, biomedicine[34], and catalysts for energy conversion[35].

In a recent experimental study, a new MBene sheet called the boridene sheet was successfully synthesized, with the formula $Mo_{4/3}B_2T_z$ (T_z denotes O, F, or OH surface terminations)[36]. The boridene sheet consists of three atomic layers arranged as Mo-B-Mo. Unlike previously reported MXene and MBene sheets, the boridene sheet exhibits ordered Mo vacancies above and below the B layer, which result from the selective etching of Y atoms in the bulk phases of $(Mo_{2/3}Y_{1/3})_2AlB_2$. Since vacancies substantially influence the stability and physical and chemical properties of materials, it is natural to ask: How would the vacancy concentration (V_m) affect the stability of the boridene sheet? Is it possible to discover stable boridene sheets with lower energy and unique properties?

In this study, we systematically investigated the stable phases and properties of boridene sheets with varying V_m. Our study begins by analyzing the vacancy-dependent stabilities of the experimentally realized Mo_4B_6 boridene sheet. We found that the vacancy-free configuration, namely the Mo_6B_6 structure, exhibits lower cohesive energy (E_{co}) than Mo_4B_6. We then expanded our study to explore the stabilities of Mo_6B_6 and its derivatives by replacing Mo with Ta, Nb, or W atoms. We totally considered twenty-four possible $M_6B_6T_6$ phases and examined their phonon spectrum and ab initio molecular dynamics (AIMD) results. We have identified six $M_6B_6T_6$ (M = Mo, Nb, Ta, and W, T = O, F, and OH) sheets with high stabilities: $Mo_6B_6O_6$, $Mo_6B_6(OH)_6$, $Nb_6B_6F_6$, $Ta_6B_6F_6$, $Ta_6B_6O_6$ and $W_6B_6O_6$. Electronic property analysis indicates these materials exhibit metallic properties and display good conductivity. Notably, boridene sheets, including $Mo_6B_6O_6$, $Mo_6B_6(OH)_6$, and $Ta_6B_6O_6$, demonstrate high catalytic activity for the hydrogen evolution reaction (HER), with near-zero Gibbs free energies of hydrogen binding. Additionally, the catalytic performance of $Nb_6B_6F_6$

and $W_6B_6O_6$ monolayers can be activated when they are negatively charged. The high stability and excellent catalytic properties of the $M_6B_6T_6$ sheets make them the competitive candidates in the MBene family for potential energy application.

MATERIALS AND METHODS

Our first-principles calculations were based on density functional theory (DFT) and implemented in the Vienna ab initio simulation package (VASP)[37]. The interactions between the ionic cores and the valence electrons were described by the projector-augmented-wave (PAW)[38] method. Electrons in the brackets of Mo[$4d^5 5s^1$], Nb[$4d^4 5s^1$], Ta[$5d^3 6s^2$], W[$5d^4 6s^2$], H[$1s^1$], O[$2s^2 2p^4$] and F[$2s^2 2p^5$] are treated as valence electrons. The Perdew-Burke-Ernzerhof functional (PBE)[39] within the generalized gradient approximation (GGA) was used throughout our computations. The energy cut off of the plane waves was set to 400 eV. The structures were completely relaxed, and the numerical convergence was achieved with a tolerance of 0.005 eV/Å in force and 10^{-6} eV in energy. The Monkhorst pack k-point grid of 7 × 7 × 1 and 14 × 14 × 1 was used for geometric optimization and self-consistent calculation, respectively. To avoid artificial interactions between the neighboring layers, we set the vacuum slab larger than 20 Å in the z-direction. The phonon spectrum was calculated based on the density functional perturbation theory using the PHONOPY package[40]. In phonon calculations, tighter convergence criteria (0.002 eV/Å for force and 10^{-8} eV for energy) with a finer k-point grid ($2\pi \times 0.02$ Å^{-1}) were employed. The AIMD simulations were performed using the canonical ensemble with temperature controlled by a Nosé-Hoover bash scheme[41]. The time scale is set to 5 ps with a time step of 1.0 fs.

The strain ε is defined as $\varepsilon = (a - a_0)/a_0$, where a is the lattice parameter in the strained state and a_0 represents that for the strain-free state. The total HER pathway can be written as $H^+ + e^- \rightarrow 1/2H_2$[42]. The Gibbs free energy (ΔG_H^*) of hydrogen atom adsorption is the critical descriptor for hydrogen evolution,[43,44] defined as $\Delta G_{H^*} = \Delta E_H + \Delta E_{ZPE} - T\Delta S_H$, where ΔE_H, E_{ZPE}, and ΔS_H are the hydrogen chemisorption energy, the reaction zero-point energy, and the entropy change between the adsorbed state and the gas phase, respectively. As $E_{ZPE} - T\Delta S_H = 0.24$ eV is a well-established approximation[42], we simplify the ΔG_H^* as $\Delta G_{H^*} = \Delta E_H + 0.24$.

RESULTS AND DISCUSSION

Vacancy concentrations of boridene sheets

Vacancies are inherent point defects in the experimentally realized crystal structures. V_m substantially affects the heat transport of atoms, thus influencing the electronic, thermal, and magnetic engineering properties of materials. Experimentally, vacancy defects in 2D materials can be deliberately produced during post-synthesis by several approaches, such as ion/electron irradiation[45], plasma treatments[46] and high-temperature annealing in the presence of different gases[47].

The pristine boridene Mo_4B_6 sheet [Figure 1A and B] crystallizes in a hexagonal lattice (space group: P321) with three atomic layers stacked as Mo-B-Mo. The centered boron layer possesses a honeycomb pattern sandwiched by two metal layers with misaligned vacancy sites. The metal atoms in pristine Mo_4B_6 are undercoordinated, making them chemically active. Previous studies[48] have shown that the bare structures are vulnerable to surface terminations such as O, OH, and F, and the functional groups tend to prefer adsorption on the bridge sites of M atoms. Therefore, the chemical formula of functionalized boridene can be expressed as $M_4B_6T_6$ (T = O, OH, F) with the unit cell containing four metal atoms, six boron atoms, and six functional groups.

Different from previously reported 2D materials such as graphene, transition metal dichalcogenides, and MXenes, whose pristine structures are vacancy-free, the synthesized boridene contains two Mo vacancies in

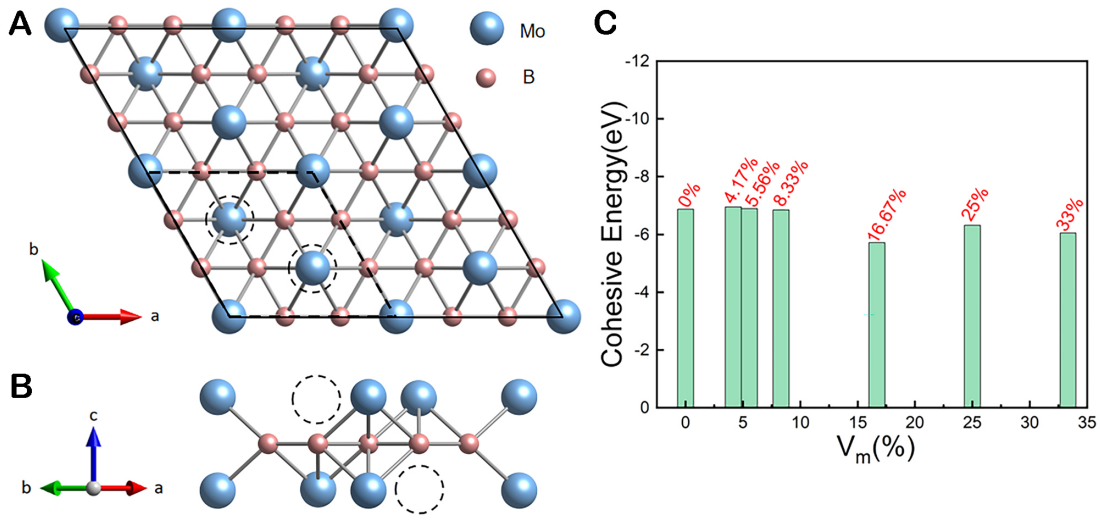

Figure 1. (A and B) Top view and side view of the Mo_4B_6 sheet. The vacancy sites are indicated by dashed circles. (C) Computed Cohesive energies of boridene sheets with different vacancy concentrations (V_m).

a unit cell [Figure 1B]. To explore the effect of vacancy defects on the stabilities of the boridene sheet, different concentrations of Mo and B vacancies were considered in 1 × 2, 1 × 3 and 2 × 2 supercells.

We defined the V_m of pristine Mo_4B_6 as the ratio of vacancies to the total number of atoms. Therefore, the metal V_m of the pristine structure is 2/12 (16.67%). Initially, we increased the metal vacancies by removing one or two Mo atoms from a unit cell. This resulted in Mo_3B_6 and Mo_2B_6 with the V_m values of 3/12 (25%) and 4/12 (33%), respectively. Noticeably, the two cases exhibit various structural configurations with multiple defects. In Supplementary Figures 1 and 2, we have depicted the potential positions of vacancies in each phase and computed their respective formation energies. Further investigations were carried out exclusively on the structure with the lowest energy.

Next, we aim to reduce the V_m in the structure. This can be achieved by either introducing additional atoms into the primitive cell (such as Mo_5B_6 and Mo_6B_6) or by removing atoms from the larger supercells (such as $Mo_{10}B_{12}$, $Mo_{16}B_{18}$, and $Mo_{22}B_{24}$ in a 1 × 2, 1 × 3 and 2 × 2 supercell, respectively [Supplementary Figures 3 and 4]. The V_m ranges from 0% to 33.3%, and then all lattices were fully relaxed to their lowest energy configurations. The geometric parameters, including lattice constants, Mo-B distances, average B-B bond lengths, energy values, and E_{co} for each defective structure, were summarized in Table 1.

The stability of the defective structures was assessed by calculating their E_{co}, defined as:

$$E_{co} = [E(Mo_xB_y) - xE(Mo) - yE(B)]/(x + y)$$

where $E(Mo_xB_y)$ is the total energies of the 2D sheets, and E(Mo) and E(B) are the energy of isolated Mo and B atoms, respectively. Taking the pristine Mo_4B_6 sheet as the reference (V_m = 16.67%), we found that the change of V_m decreases E_{co} [Figure 1C, Table 1], indicating the enhancement of material stability. For example, the E_{co} of vacancy-free boridene Mo_6B_6 is -6.87 eV/atom, lower than many other transition metal borides such as FeB_2 (-4.87 eV/atom)[49], FeB_3 (-5.93 eV/atom)[50], and FeB_6 (-5.79 eV/atom)[51] monolayers.

Table 1. Lattice constants a and b (in Å), average bond length for Mo-B and B-B (in Å), the vacancy concentrations (V_m) and cohesive energy (in eV per atom) for different structures

Formula	a	b	Mo-B	B-B	V_m (%)	Cohesive energy
Mo_2B_6	5.22	5.22	2.15	1.78	33.33	-6.09
Mo_3B_6	5.13	5.13	2.22	1.70	25	-6.32
Mo_4B_6	5.17	5.17	2.29	1.79	16.67	-5.72
Mo_5B_6	5.38	5.38	2.29	1.79	8.33	-6.86
Mo_6B_6	5.38	5.38	2.29	1.79	0	-6.87
$Mo_{10}B_{12}$	10.53	5.28	2.30	1.78	8.33	-6.83
$Mo_{16}B_{18}$	15.90	5.28	2.26	1.76	5.56	-6.90
$Mo_{22}B_{24}$	10.77	10.77	2.28	1.78	4.17	-6.95

Stabilities of boridene sheets and its derivatives

To further identify the dynamical stability of boridene sheets with different defect concentrations, the phonon spectrum for each structure was calculated. Previous research has demonstrated that the bare Mo_4B_6 sheet is highly unstable. However, introducing functional groups (-OH, -O, -F) on its surfaces has proven to significantly enhance its stability[48]. By employing a similar approach, we conducted phonon spectrum calculations for Mo_5B_6, Mo_6B_6, $Mo_{10}B_{12}$, $Mo_{16}B_{18}$, and $Mo_{22}B_{24}$ sheets with various functional groups. We found that the vacancy-free Mo_6B_6 layers [Supplementary Figure 5] functionalized with -O and -OH groups, namely $Mo_6B_6O_6$ and $Mo_6B_6(OH)_6$ sheets, become stable with no soft modes in the calculated phonon spectra, as shown in Figure 2A and B. Importantly, the highest frequencies of $Mo_6B_6O_6$ are up to 28.1 THz (937 cm^{-1}), higher than that found in silicene (580 cm^{-1})[52], MoS_2 (473 cm^{-1})[53] and Cu_2Si (420 cm^{-1})[54] monolayers. The high-energy phonons indicate the robust Mo-B and B-O interactions in the boridene sheets.

We further evaluated their thermal stabilities by conducting AIMD simulations at 300 K over the time scale of at least 5 ps. Analysis of the snapshots captured at the end of AIMD simulation reveals the excellent preservation of both hexagonal frameworks, with no observable fractures in chemical bonds [Figure 3A and B]. This finding further confirms the thermodynamic stability of both $Mo_6B_6O_6$ and $Mo_6B_6(OH)_6$ sheets.

The above analysis not only demonstrates the high stability of the vacancy-free $Mo_6B_6T_6$ sheets but also indicates that these materials exhibit even lower formation energy than the experimentally synthesized boridene sheets. This suggests that the vacancy-free boridene sheets hold great promise for future experimental validation.

The high stability of the Mo_6B_6 framework has prompted us to further explore whether other transition metals can stabilize this structure. To investigate this, we replaced Mo with neighboring transition metals, such as Nb, W, and Ta, from the periodic table. We performed dynamical and thermal stability tests on the functionalized $M_6B_6T_6$ sheets (M = Nb, W, or Ta and T = O, OH, or F). As a result, we additionally identified four $M_6B_6T_6$ sheets, namely $Nb_6B_6F_6$, $Ta_6B_6F_6$, $Ta_6B_6O_6$, and $W_6B_6O_6$, to be very stable (see Figure 2C-F, Figure 3C-F). Although a $W_6B_6(OH)_6$ sheet displays dynamical stability, its thermodynamic instability prompts us to exclude it from further discussion. However, we have included its structural and electronic properties in the Supplementary Material [Supplementary Figures 6 and 7, Supplementary Table 1].

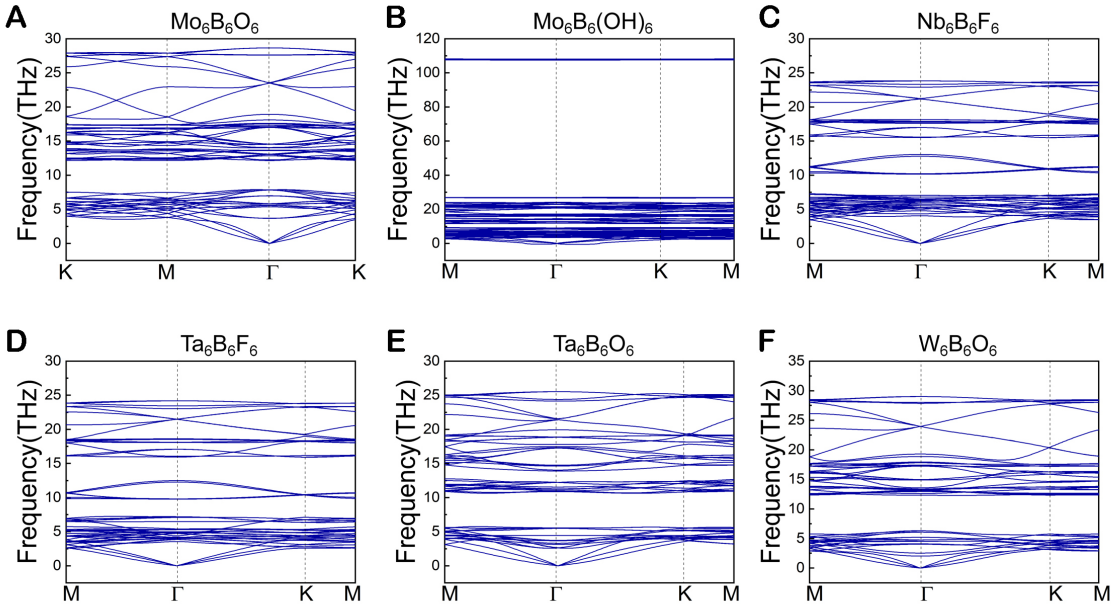

Figure 2. (A-F) Phonon spectrum of different $M_6B_6T_6$ (M = Mo, Nb, Ta, W, T = O, F, OH) sheets.

Bonding and charge analysis

We have identified six stable $M_6B_6T_6$ sheets, in which the element M can be Mo, Nb, W, or Ta, and the terminal T can be -O, -OH, or -F. The lattice parameters and E_{co} for these structures are summarized in Table 2. Noticeably, the E_{co} values range from -5.79 to -7.50 eV, lower than many previously reported boron-based layers[49,50,55,56].

To gain a deeper understanding of the high stability exhibited by the functionalized $M_6B_6T_6$ sheets, we have calculated the electron localization function (ELF) for all these sheets, as shown in Figure 4. For the bare M_6B_6 layers, the electron localization is predominantly located between the boron atoms, indicating the presence of covalent bonds between B-B atoms. The absence of electron localization between the metal and boron atoms suggests the existence of ionic bonds in these regions. In the case of the functionalized $M_6B_6T_6$ layers, a larger ELF is observable between the B-B atoms in most structures, implying the strengthening of the B-B bonds. Interestingly, a considerable electron localization is observed around the functional groups, demonstrating that the surfaces of $M_6B_6T_6$ layers are chemically inert compared to the pristine M_6B_6 sheets. Among the six $M_6B_6T_6$ sheets, we found a higher electron population concentrated around the B atoms and functional groups in the $Ta_6B_6O_6$ and $W_6B_6O_6$ sheets [Figure 4I and J]. This suggests stronger bonding interactions in the two sheets. This is consistent with the calculated E_{co}, as the $Ta_6B_6O_6$ and $W_6B_6O_6$ sheets exhibit the lowest values among all the sheets [Table 2].

The Bader charge analysis reveals a significant electron transfer from the metal elements to the O, OH, and F terminals, with a range of 0.85-1.33 e (see the details in Supplementary Figure 8-13). This finding confirms that the functional groups can compensate for the extra electrons on the surface of the pristine M_6B_6 sheets, thereby greatly enhancing their structural stability.

Table 2. Lattice constants (in Å) and cohesive energies (in eV) of different $M_6B_6T_6$ sheets

System	a	b	Cohesive energy
$Mo_6B_6O_6$	5.11	5.11	-6.98
$Mo_6B_6(OH)_6$	5.46	5.26	-5.79
$Ta_6B_6O_6$	5.29	5.29	-7.50
$Ta_6B_6F_6$	5.39	5.39	-6.70
$W_6B_6O_6$	5.09	5.09	-7.38
$Nb_6B_6F_6$	5.39	5.39	-6.41

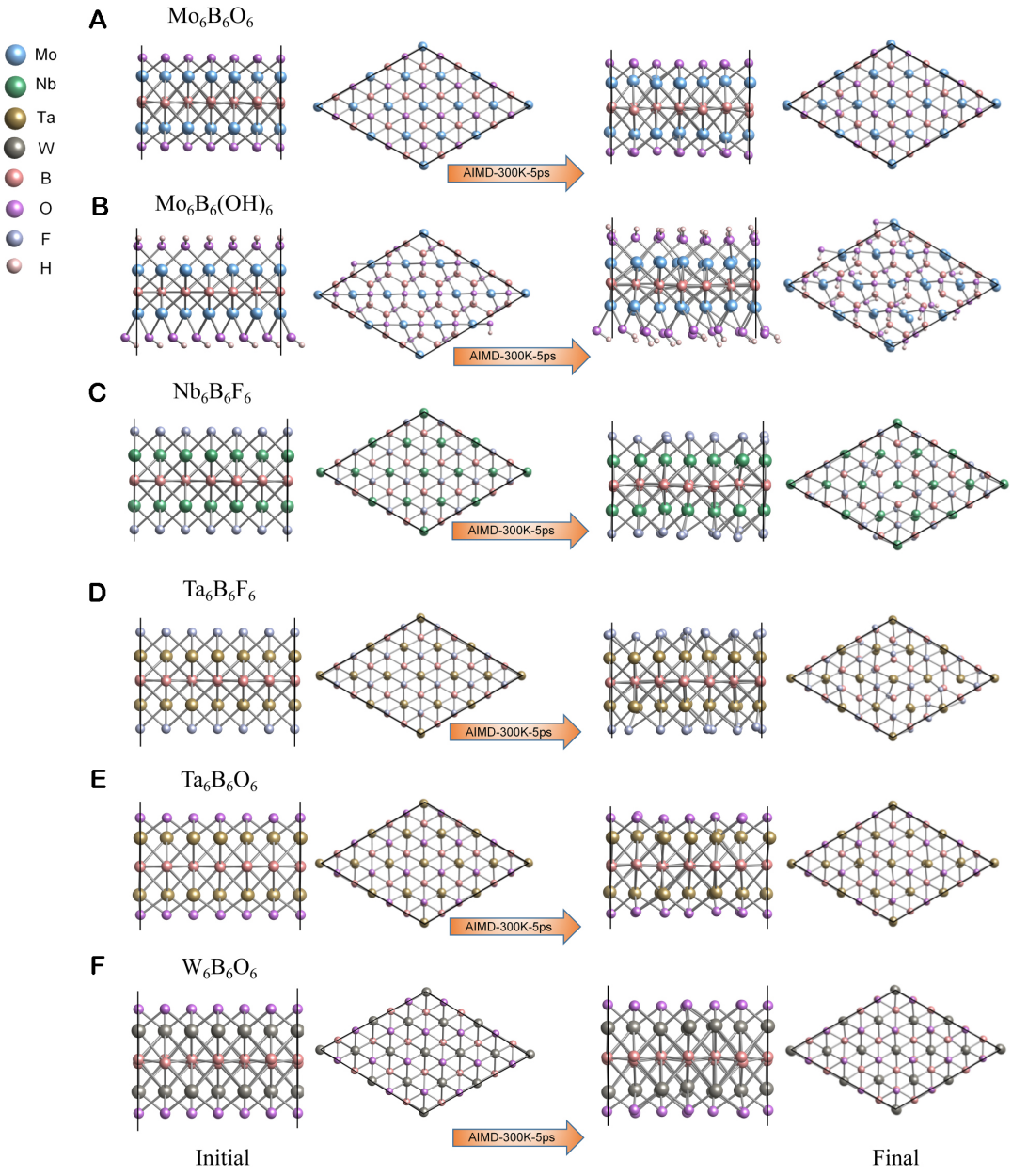

Figure 3. AIMD simulated results for different $M_6B_6T_6$ (M = Mo, Nb, Ta, W, T = O, F, OH) sheets at 300 K for 5 ps.

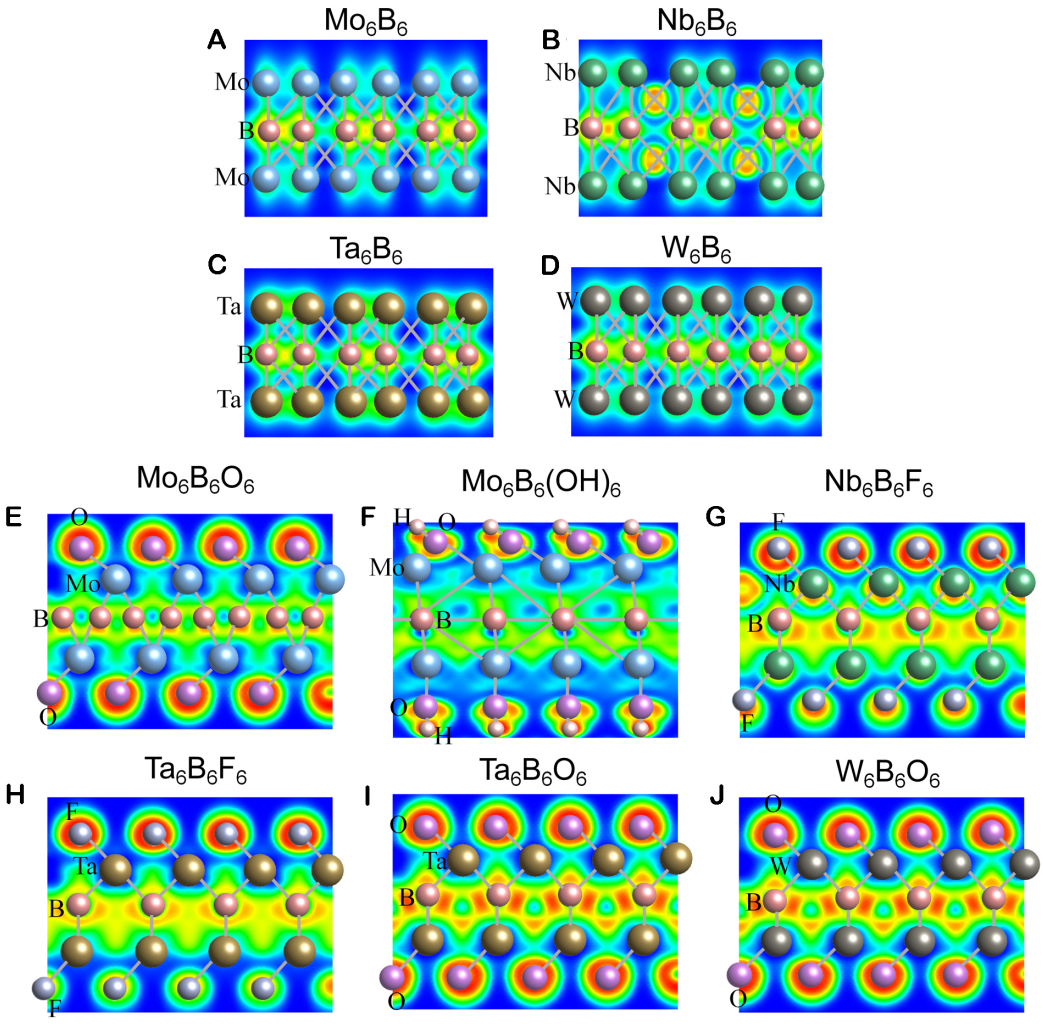

Figure 4. The slice cuts of ELF along the (001) plane for (A-D) the bare M_6B_6 sheets and (E-J) functionalized $M_6B_6T_6$ sheets. The isovalue was set to 0.75 eÅ^{-3}.

Mechanical properties

The mechanical properties of the functionalized $M_6B_6T_6$ sheets were analyzed by calculating the elastic constants. According to the elastic stability criteria[57], a stable 2D hexagonal sheet should satisfy $C_{44} > 0$ and $C_{11} > |C_{12}|$, where C_{ij} is the elastic constants. For all $M_6B_6T_6$ sheets, the calculated values of C_{ij} [Table 3] indicate that these mechanical stability criteria are fully satisfied. Additionally, the estimated Poisson's ratios, ν, are all positive, ranging from 0.098 to 0.3. The estimated Young's modulus (213.55~338.32 GPa·nm) is generally higher than that of phosphorene (23~92.3 GPa·nm)[58] and monolayer Be_5C_2 (33~130 GPa·nm)[59]. However, it is similar to the Young's modulus of MoS_2 (~270 GPa)[60] and WS_2 (244.18 GPa)[61].

Furthermore, our study reveals that the V_m significantly affects the mechanical properties of the Mo_xB_y sheets. By computing the elastic constants [Supplementary Table 2], we found a significant alteration in Poisson's ratio due to different V_m. Specifically, this ratio varied from ν = 0.14 for Mo_2B_6 to ν = 0.35 for

Table 3. Calculated elastic constants (in N/m), the Poisson's ratio ν, and the Young's modulus (in GPa·nm) for all structures

System	C_{11}	C_{22}	C_{12}	C_{44}	ν	Young's modulus
$Mo_6B_6O_6$	130.13	133.99	12.7	59.92	0.098	292.05
$Mo_6B_6(OH)_6$	82.63	105.67	23.02	34.67	0.28	218.37
$Ta_6B_6O_6$	151.86	149.83	45.03	52.45	0.3	304.33
$Ta_6B_6F_6$	106.06	105.13	30.33	37.47	0.29	214.08
$W_6B_6O_6$	156.76	157.84	25.21	66.29	0.16	338.32
$Nb_6B_6F_6$	103.05	102.50	24.77	39.31	0.24	213.55

Mo_4B_6. In the absence of vacancies, the Young's modulus exhibited the highest value. However, introducing vacancies reduced the Young's modulus. For instance, in the Mo_4B_6 case, the Young's modulus was reduced to 101.57 GPa•nm. Despite the decrease in Young's modulus in the defective Mo_xB_y sheets, it still surpasses that of phosphorene.

Electronic properties

Next, we analyze how the electronic properties of $M_6B_6T_6$ are influenced by surface functionalization and composition. Figure 5 presents the calculated band structures for six different $M_6B_6T_6$ sheets. The band structures revealed that all sheets exhibit metallic characteristics, similar to borophene[62] and some MXenes such as V_2C and Nb_2C[63]. The band dispersions of $M_6B_6T_6$ were strongly affected by the surface terminals and different metal elements. For instance, the band structure of $Mo_6B_6(OH)_6$ [Figure 5B] shows the existence of two band crossing points along the M-Γ-K lines, while these points disappear with the surface -O termination [Figure 5A]. Dirac points can be observed in $W_6B_6O_6$ [Figure 5F], but they do not exist when the metal element is replaced with Ta [Figure 5E].

It is well-known that the PBE method can sometimes result in inaccurate electronic structures. Therefore, we employed the Heyd-Scuseria-Ernzerhof (HSE) method to obtain more accurate electronic properties. As depicted in Supplementary Figure 14, the band dispersion of each material is similar to that of the PBE results, and the Dirac points in $Mo_6B_6(OH)_6$ and $W_6B_6O_6$ are well-preserved, further confirming the previous analysis. Importantly, the metallic electronic properties of these structures also indicate excellent conductivity, making them suitable for applications in electronics and catalysis (which we will discuss in detail later). These properties are similar to those observed in the MXene family[64] and borophene monolayer[65]. We have additionally computed the vacancy-dependent band structures for the 2D Mo_xB_y. As illustrated in Supplementary Figure 15, we have found that all Mo_xB_y sheets retain their metallic characteristics. This is rational, as vacancies can generate localized electronic states, thereby promoting the dispersion of electrons and sustaining the metallic properties.

Figure 6 illustrates the partial density of states (PDOS) for the $M_6B_6T_6$ sheets. The -O functionalized structures, namely $Mo_6B_6O_6$, $Ta_6B_6O_6$, and $W_6B_6O_6$, show that the electronic states at the Fermi level are primarily dominated by the *d* orbitals of the metal atoms with a small contribution from the O-*2p* and B-*2p* states. In contrast, the -OH and -F functionalized structures exhibit negligible contributions from the p-orbitals. Generally, the magnitude of the density of states (DOS) at the Fermi level reflects the electron configuration of the d orbitals. For instance, among the six candidates, $Mo_6B_6(OH)_6$ has the largest DOS at the Fermi level, which can be attributed to its electron configuration of $4d^5$. In comparison, $Ta_6B_6O_6$ has the lowest DOS due to its $5d^3$ electron configuration in the outer shell.

HER activity

By analyzing the DOS, we found that the predicted vacancy-free boridene sheets exhibit metallic properties

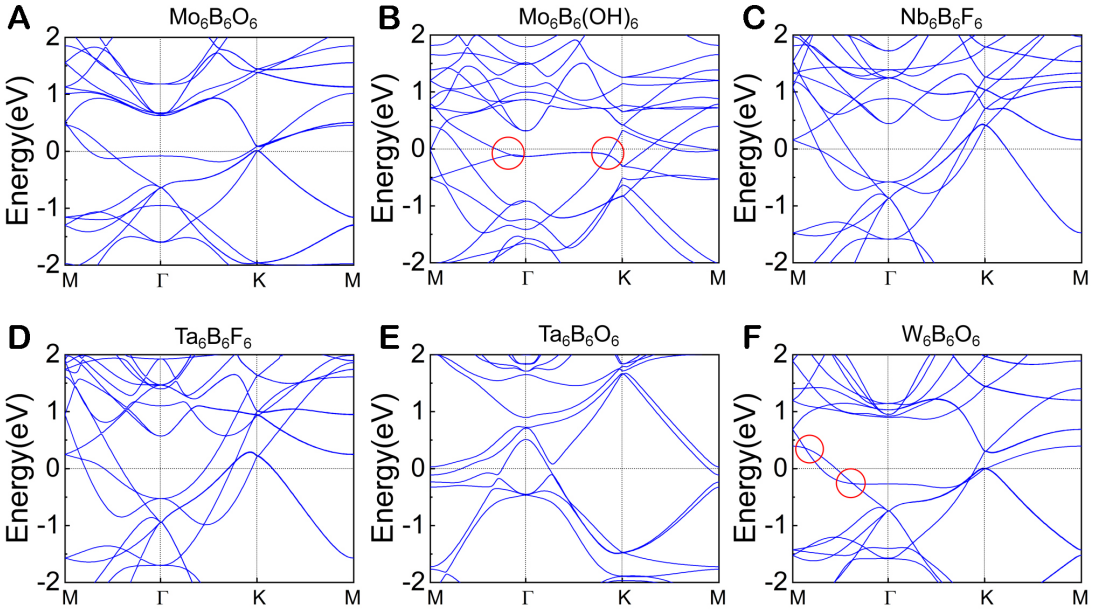

Figure 5. (A-F) Band structures of different $M_6B_6T_6$ sheets. Red circles locate the band crossing points near the Fermi level.

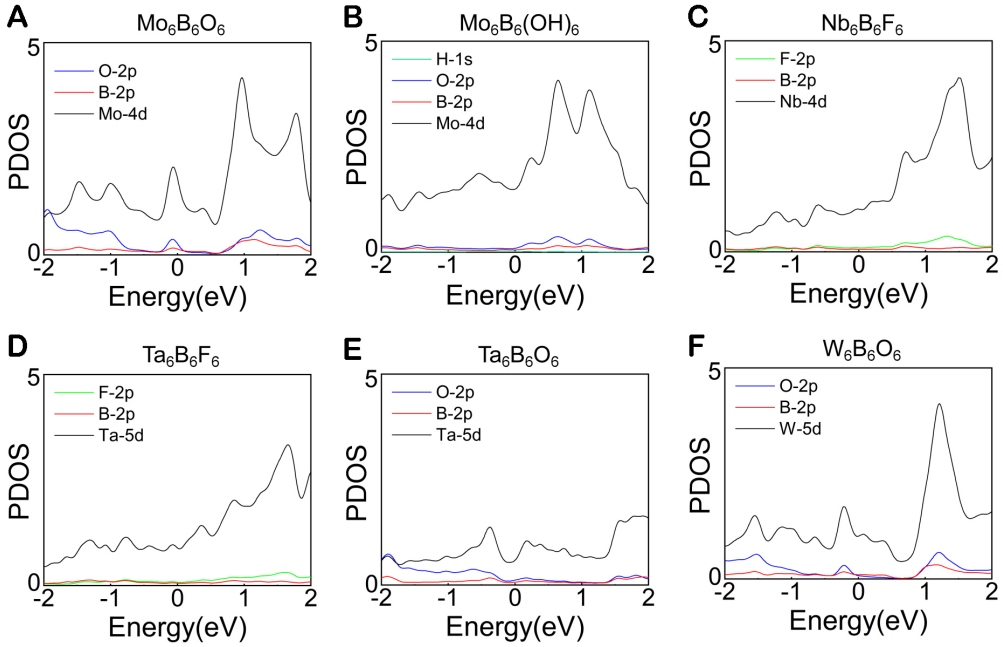

Figure 6. (A-F) Partial density of states (PDOS) of different $M_6B_6T_6$ sheets.

and have significant DOS at the Fermi level. This suggests that the material has good conductivity, which could be advantageous for electrocatalytic processes. To investigate their potential as electrocatalysts, we mainly focus on their HER performance in the subsequent discussion. HER catalysts have been extensively studied in 2D materials, not only in the monolayer forms such as MBene and MXene but also in the

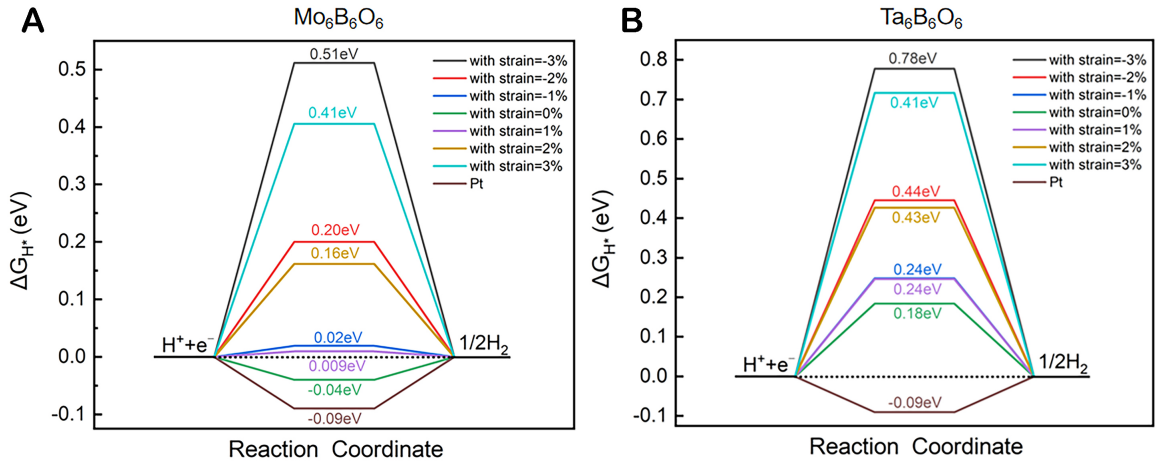

Figure 7. Gibbs free energy (ΔG_{H}^*) at the O sites of the (A) $Mo_6B_6O_6$ and (B) $Ta_6B_6O_6$ monolayers under different strains (ε).

heterostructures including N-doped graphene-based systems[35]. Hybridizing two types of 2D materials would lead to strong interlayer coupling, thus enhancing the HER performance, as exemplified in the N-doped graphene/MXenes composites[66]. Generally, the HER catalytic activity of a catalyst is closely connected to the adsorption and desorption processes of individual hydrogen atoms on its surface. To be an ideal catalyst for HER, the binding strength of the catalytic site with high HER properties should neither be too weak nor too strong. Hence, the ΔG_{H^*} for an ideal HER catalyst should be close to 0. A positive ΔG_{H^*} indicates low kinetics of hydrogen adsorption, while a negative value hampers the kinetics of hydrogen molecule release.

We calculated ΔG_{H^*} by testing different surface sites of vacancy-free boridenes. Among the six stable configurations, three are active for HER, including $Mo_6B_6O_6$, $Ta_6B_6O_6$, and $Mo_6B_6(OH)_6$. We found that the O atoms of $Mo_6B_6O_6$ and $Ta_6B_6O_6$ and OH group of $Mo_6B_6(OH)_6$ are active sites for HER, with the ΔG_{H^*} of -0.04, 0.18, and 0.11 eV, respectively (see Figure 7 and Supplementary Figure 16 for details). The calculated ΔG_{H^*} for $Mo_6B_6O_6$ is even better than that of Pt (ΔG_{H^*} = -0.09 eV), and comparable to that of the 2D MXenes such as Ti_2CO_2 (ΔG_{H^*} = -0.04), Nb_2CO_2 (ΔG_{H^*} = 0.02)[63].

As strain engineering is widely employed to modify the properties of 2D materials due to its simplicity and large adjustable range, we also explored the effect of strain on the HER performance for the above three sheets [Figure 7 and Supplementary Figure 16]. Experimentally, lattice strain can be readily applied for 2D materials by introducing stretchable substrates[67] or through doping methods[68]. We found that the strain engineering can modulate the HER performance of boridene sheets. Taking $Mo_6B_6O_6$ as an example [Figure 7A], the tensile strain drives ΔG_{H^*} toward a more positive value, reducing the catalytic performance. On the contrary, a compressive strain can decrease the value of ΔG_{H^*}. Remarkably, applying a small strain of 1% can significantly enhance the HER performance of the O sites with the ΔG_{H^*} of 0.009 eV. $Nb_6B_6F_6$ and $W_6B_6O_6$ sheets are inactive for the HER due to the large ΔG_{H^*} under neutral conditions. We find that injecting a small extra charge can greatly improve their HER performance. Specifically, applying a negative charge density of 0.05-0.06 e/atom can reduce the ΔG_{H^*} for $Nb_6B_6F_6$ and $W_6B_6O_6$ to 0.1 and 0.09 eV, respectively, as shown in Supplementary Figure 17, making them suitable for H_2 production.

As V_m can usually modulate the HER activity of 2D materials due to their ability to influence adsorption energies and affect charge transfer dynamics at the surface, we calculated the ΔG_{H^*} of the Mo_xB_y sheets with different V_m. As shown in Supplementary Figure 18, the bare Mo_4B_6 sheet (V_m = 16.67%) shows the largest ΔG_{H^*} of -0.84 eV, which is unfavorable for HER. In contrast, increasing V_m to 33% (Mo_2B_6) can greatly improve the catalytic activity of the material, with a ΔG_{H^*} of -0.14 eV, close to the ideal ΔG_{H^*} value.

CONCLUSIONS

In conclusion, through first-principles calculations, we have discovered a new type of MBene sheets, namely, the vacancy-free boridene $M_6B_6T_6$ (M = Mo, Nb, Ta, and W, T = O, F, and OH) monolayers. These structures show a lower E_{co} than the boridene Mo_4B_6 sheet, indicating higher stability. We have identified a total of six boridene sheets that are inherently metallic and their band dispersions are intricately linked to their termination groups. Importantly, five of the $M_6B_6T_6$ sheets exhibit significant catalytic activity for HER under neutral or charged conditions. Among them, the $Mo_6B_6O_6$ sheet shows the most optimal ΔG_{H^*} value of -0.04 eV. This work introduces new low-energy phases in the MBene family and highlights their potential applications in catalysis.

DECLARATIONS

Authors' contributions

Made substantial contributions to the conception and design of the study and performed data analysis and interpretation: Ma F, Jiao Y, Du A

Performed data acquisition and provided administrative, technical, and material support: Zhao Y, Zhang J, Ma F, Wu H, Meng W, Liu Y, Jiao Y, Du A

Availability of data and materials

Data will be made available upon request.

Financial support and sponsorship

This work is supported by the National Natural Science Foundation of China (Grant No. 11904077 and No. 12204144), the Natural Science Fund of Hebei Province (Grant No. A2022205027), financial support program from Hebei Province (Grant No. E2019050018, No. C20220503, and No. C20230509), Science Foundation of Hebei Normal University (Grant No. L2022B06), and the Key Program of Natural Science Foundation of Hebei Province (Grant No. A2021205024).

Conflicts of interest

All authors declared that there are no conflicts of interest.

Ethical approval and consent to participate

Not applicable.

Consent for publication

Not applicable.

REFERENCES

1. Ryu B, Wang L, Pu H, Chan MKY, Chen J. Understanding, discovery, and synthesis of 2D materials enabled by machine learning. *Chem Soc Rev* 2022;51:1899-925. DOI

2. Qiu HJ, Ito Y, Cong W, et al. Nanoporous graphene with single-atom nickel dopants: an efficient and stable catalyst for electrochemical hydrogen production. *Angew Chem Int Ed* 2015;54:14031-5. DOI
3. Zhang Y, Ugeda MM, Jin C, et al. Electronic structure, surface doping, and optical response in epitaxial WSe_2 thin films. *Nano Lett* 2016;16:2485-91. DOI
4. Jia Y, Zhang L, Gao G, et al. A heterostructure coupling of exfoliated Ni-Fe hydroxide nanosheet and defective graphene as a bifunctional electrocatalyst for overall water splitting. *Adv Mater* 2017;29:1700017. DOI
5. Gogotsi Y, Huang Q. MXenes: two-dimensional building blocks for future materials and devices. *ACS Nano* 2021;15:5775-80. DOI PubMed
6. Jiang Z, Wang P, Jiang X, Zhao J. MBene (MnB): a new type of 2D metallic ferromagnet with high Curie temperature. *Nanoscale Horiz* 2018;3:335-41. DOI PubMed
7. Feng S, Miao N, Wang J. Hexagonal MBene (Hf_2BO_2): a promising platform for the electrocatalysis of hydrogen evolution reaction. *ACS Appl Mater Interfaces* 2021;13:56131-9. DOI PubMed
8. Li Y, Li L, Huang R, Wen Y. Computational screening of MBene monolayers with high electrocatalytic activity for the nitrogen reduction reaction. *Nanoscale* 2021;13:15002-9. DOI
9. Michałowski PP, Anayee M, Mathis TS, et al. Oxycarbide MXenes and MAX phases identification using monoatomic layer-by-layer analysis with ultralow-energy secondary-ion mass spectrometry. *Nat Nanotechnol* 2022;17:1192-7. DOI
10. Zhou S, Yang X, Pei W, Jiang Z, Zhao J. MXene and MBene as efficient catalysts for energy conversion: roles of surface, edge and interface. *J Phys Energy* 2021;3:012002. DOI
11. Bhat A, Anwer S, Bhat KS, Mohideen MIH, Liao K, Qurashi A. Prospects challenges and stability of 2D MXenes for clean energy conversion and storage applications. *npj 2D Mater Appl* 2021;5:1-21. DOI
12. Li X, Huang Z, Shuck CE, Liang G, Gogotsi Y, Zhi C. MXene chemistry, electrochemistry and energy storage applications. *Nat Rev Chem* 2022;6:389-404. DOI PubMed
13. Pang J, Chang B, Liu H, Zhou W. Potential of MXene-based heterostructures for energy conversion and storage. *ACS Energy Lett* 2022;7:78-96. DOI
14. Shukla V. The tunable electric and magnetic properties of 2D MXenes and their potential applications. *Mater Adv* 2020;1:3104-21. DOI
15. Gogotsi Y, Anasori B. The rise of MXenes. *ACS Nano* 2019;13:8491-4. DOI PubMed
16. Anasori B, Lukatskaya MR, Gogotsi Y. 2D metal carbides and nitrides (MXenes) for energy storage. *Nat Rev Mater* 2017;2:16098. DOI
17. Khazaei M, Ranjbar A, Arai M, Sasaki T, Yunoki S. Electronic properties and applications of MXenes: a theoretical review. *J Mater Chem C* 2017;5:2488-503. DOI
18. Wang H, Wu Y, Yuan X, et al. Clay-inspired MXene-based electrochemical devices and photo-electrocatalyst: state-of-the-art progresses and challenges. *Adv Mater* 2018;30:e1704561. DOI
19. Yu XF, Li YC, Cheng JB, et al. Monolayer Ti_2CO_2: a promising candidate for NH□ sensor or capturer with high sensitivity and selectivity. *ACS Appl Mater Interfaces* 2015;7:13707-13. DOI PubMed
20. Fu Z, Wang N, Legut D, et al. Rational design of flexible two-dimensional mxenes with multiple functionalities. *Chem Rev* 2019;119:11980-2031. DOI
21. Anand R, Ram B, Umer M, et al. Doped MXene combinations as highly efficient bifunctional and multifunctional catalysts for water splitting and metal-air batteries. *J Mater Chem A* 2022;10:22500-11. DOI
22. Zhang B, Zhou J, Sun Z. MBenes: progress, challenges and future. *J Mater Chem A* 2022;10:15865-80. DOI
23. Zhu H, Liang Z, Xue S, et al. DFT practice in MXene-based materials for electrocatalysis and energy storage: from basics to applications. *Ceram Int* 2022;48:27217-39. DOI
24. Yang X, Shang C, Zhou S, Zhao J. MBenes: emerging 2D materials as efficient electrocatalysts for the nitrogen reduction reaction. *Nanoscale Horiz* 2020;5:1106-15. DOI
25. Wang J, Liu W, Luo G, et al. Synergistic effect of well-defined dual sites boosting the oxygen reduction reaction. *Energy Environ Sci* 2018;11:3375-9. DOI
26. Zhang T, Zhang B, Peng Q, Zhou J, Sun Z. Mo_2B_2 MBene-supported single-atom catalysts as bifunctional HER/OER and OER/ORR electrocatalysts. *J Mater Chem A* 2021;9:433-41. DOI
27. Khazaei M, Wang J, Estili M, et al. Novel MAB phases and insights into their exfoliation into 2D MBenes. *Nanoscale* 2019;11:11305-14. DOI
28. Zhang H, Xiang H, Dai F, Zhang Z, Zhou Y. First demonstration of possible two-dimensional MBene CrB derived from MAB phase Cr_2AlB_2. *J Mater Sci Technol* 2018;34:2022-6. DOI
29. Alameda LT, Moradifar P, Metzger ZP, Alem N, Schaak RE. Topochemical deintercalation of Al from MoAlB: stepwise etching pathway, layered intergrowth structures, and two-dimensional MBene. *J Am Chem Soc* 2018;140:8833-40. DOI PubMed
30. Ma F, Jiao Y, Wu W, Liu Y, Yang SA, Heine T. Half-auxeticity and anisotropic transport in Pd decorated two-dimensional boron sheets. *Nano Lett* 2021;21:2356-62. DOI
31. Gao Z, Wang Q, Wu W, et al. Monolayer RhB4: half-auxeticity and almost ideal spin-orbit Dirac point semimetal. *Phys Rev B* 2021;104:245423. DOI
32. Jiao Y, Ma F, Zhang X, Heine T. A perfect match between borophene and aluminium in the AlB_3 heterostructure with covalent Al-B

bonds, multiple Dirac points and a high Fermi velocity. *Chem Sci* 2022;13:1016-22. DOI PubMed PMC

33. Gao Z, Ma F, Wu H, et al. Two-dimensional ruthenium boride: a Dirac nodal loop quantum electrocatalyst for efficient hydrogen evolution reaction. *J Mater Chem A* 2023;11:3717-24. DOI
34. Xiao Y, Li Y, Guo Z, et al. Functionalized Mo_2B_2 MBenes: promising anchoring and electrocatalysis materials for lithium-sulfur battery. *Appl Surf Sci* 2021;566:150634. DOI
35. Zhou S, Yang X, Pei W, Jiang Z, Zhao J. MXene and MBene as efficient catalysts for energy conversion: roles of surface, edge and interface. *J Phys Energy* 2021;3:012002. DOI
36. Zhou J, Palisaitis J, Halim J, et al. Boridene: two-dimensional $Mo_{4/3}B_{2-x}$ with ordered metal vacancies obtained by chemical exfoliation. *Science* 2021;373:801-5. DOI
37. Kresse G, Furthmüller J. Efficient iterative schemes for ab initio total-energy calculations using a plane-wave basis set. *Phys Rev B Condens Matter* 1996;54:11169-86. DOI PubMed
38. Blöchl PE. Projector augmented-wave method. *Phys Rev B Condens Matter* 1994;50:17953-79. DOI PubMed
39. Perdew JP, Burke K, Ernzerhof M. Generalized gradient approximation made simple. *Phys Rev Lett* 1996;77:3865-8. DOI PubMed
40. Togo A, Oba F, Tanaka I. First-principles calculations of the ferroelastic transition between rutile-type and $CaCl_2$ -type SiO_2 at high pressures. *Phys Rev B* 2008:78. DOI
41. Martyna GJ, Klein ML, Tuckerman M. Nosé-Hoover chains: the canonical ensemble via continuous dynamics. *J Chem Phys* 1992;97:2635-43. DOI
42. Noerskov JK, Bligaard T, Logadottir A, et al. Trends in the exchange current for hydrogen evolution. *ChemInform* 2005;36:chin. 200524023. DOI
43. Conway BE, Bockris JOM. The adsorption of hydrogen and the mechanism of the electrolytic hydrogen evolution reaction. *Naturwissenschaften* 1956;43:446. DOI
44. Parsons R. The rate of electrolytic hydrogen evolution and the heat of adsorption of hydrogen. *Trans Faraday Soc* 1958;54:1053. DOI
45. Schwartz J, Aloni S, Ogletree DF, Schenkel T. Effects of low-energy electron irradiation on formation of nitrogen-vacancy centers in single-crystal diamond. *New J Phys* 2012;14:043024. DOI
46. Tong B, Meng G, Deng Z, Horprathum M, Klamchuen A, Fang X. Surface oxygen vacancy defect engineering of p-$CuAlO_2$ *via* Ar&H $_2$ plasma treatment for enhancing VOCs sensing performances. *Chem Commun* 2019;55:11691-4. DOI PubMed
47. Lin Z, Carvalho BR, Kahn E, et al. Defect engineering of two-dimensional transition metal dichalcogenides. *2D Mater* 2016;3:022002. DOI
48. Wu H, Gao Z, Ma F, et al. Surface functionalization of two-dimensional boridene family: enhanced stability, tunable electronic property, and high catalytic activity. *Appl Surf Sci* 2022;602:154374. DOI
49. Zhang H, Li Y, Hou J, Du A, Chen Z. Dirac state in the FeB_2 monolayer with graphene-like boron sheet. *Nano Lett* 2016;16:6124-9. DOI
50. Tang C, Ostrikov KK, Sanvito S, Du A. Prediction of room-temperature ferromagnetism and large perpendicular magnetic anisotropy in a planar hypercoordinate FeB_3 monolayer. *Nanoscale Horiz* 2021;6:43-8. DOI
51. Zhang H, Li Y, Hou J, Tu K, Chen Z. FeB_6 monolayers: the graphene-like material with hypercoordinate transition metal. *J Am Chem Soc* 2016;138:5644-51. DOI
52. Cahangirov S, Topsakal M, Aktürk E, Sahin H, Ciraci S. Two- and one-dimensional honeycomb structures of silicon and germanium. *Phys Rev Lett* 2009;102:236804. DOI PubMed
53. Molina-sánchez A, Wirtz L. Phonons in single-layer and few-layer MoS_2 and WS_2. *Phys Rev B* 2011;84:155413. DOI
54. Yang LM, Bačić V, Popov IA, et al. Two-dimensional Cu_2Si monolayer with planar hexacoordinate copper and silicon bonding. *J Am Chem Soc* 2015;137:2757-62. DOI
55. Sun Y, Zhuo Z, Wu X, Yang J. Room-temperature ferromagnetism in two-dimensional Fe_2Si nanosheet with enhanced spin-polarization ratio. *Nano Lett* 2017;17:2771-7. DOI
56. Wu X, Dai J, Zhao Y, Zhuo Z, Yang J, Zeng XC. Two-dimensional boron monolayer sheets. *ACS Nano* 2012;6:7443-53. DOI PubMed
57. Wu Z, Zhao E, Xiang H, Hao X, Liu X, Meng J. Crystal structures and elastic properties of superhard IrN_2 and IrN_3 from first principles. *Phys Rev B* 2007;76:054115. DOI
58. Wang L, Kutana A, Zou X, Yakobson BI. Electro-mechanical anisotropy of phosphorene. *Nanoscale* 2015;7:9746-51. DOI PubMed
59. Wang Y, Li F, Li Y, Chen Z. Semi-metallic Be_5C_2 monolayer global minimum with quasi-planar pentacoordinate carbons and negative Poisson's ratio. *Nat Commun* 2016;7:11488. DOI PubMed PMC
60. Bertolazzi S, Brivio J, Kis A. Stretching and breaking of ultrathin MoS_2. *ACS Nano* 2011;5:9703-9. DOI PubMed
61. Li J, Medhekar NV, Shenoy VB. Bonding charge density and ultimate strength of monolayer transition metal dichalcogenides. *J Phys Chem C* 2013;117:15842-8. DOI
62. Mannix AJ, Zhou XF, Kiraly B, et al. Synthesis of borophenes: anisotropic, two-dimensional boron polymorphs. *Science* 2015;350:1513-6. DOI PubMed PMC
63. Gao G, O'mullane AP, Du A. 2D MXenes: a new family of promising catalysts for the hydrogen evolution reaction. *ACS Catal* 2017;7:494-500. DOI
64. Volmer F, Ersfeld M, Faria Junior PE, et al. Twist angle dependent interlayer transfer of valley polarization from excitons to free charge carriers in WSe_2/$MoSe_2$ heterobilayers. *npj 2D Mater Appl* 2023;7:58. DOI

65. Kaneti YV, Benu DP, Xu X, Yuliarto B, Yamauchi Y, Golberg D. Borophene: two-dimensional boron monolayer: synthesis, properties, and potential applications. *Chem Rev* 2022;122:1000-51. DOI PubMed
66. Zhou S, Yang X, Pei W, Liu N, Zhao J. Heterostructures of MXenes and N-doped graphene as highly active bifunctional electrocatalysts. *Nanoscale* 2018;10:10876-83. DOI
67. Conley HJ, Wang B, Ziegler JI, Haglund RF Jr, Pantelides ST, Bolotin KI. Bandgap engineering of strained monolayer and bilayer MoS_2. *Nano Lett* 2013;13:3626-30. DOI PubMed
68. Xu X, Liang T, Kong D, Wang B, Zhi L. Strain engineering of two-dimensional materials for advanced electrocatalysts. *Mater Today Nano* 2021;14:100111. DOI